

Parton distributions extracted from data on deep-inelastic lepton scattering, prompt photon production, and the Drell-Yan process

P. N. Harriman, A. D. Martin, and W. J. Stirling
Department of Physics, University of Durham, Durham DH1 3LE, England

R. G. Roberts
Rutherford Appleton Laboratory, Chilton, Didcot OX11 0QX, England
 (Received 6 February 1990)

We present a next-to-leading-order QCD structure-function analysis of deep-inelastic muon and neutrino scattering data. In particular, we incorporate new $F_2^{\mu n}/F_2^{\mu p}$ data and take account of a recent reanalysis of SLAC data. The fit is performed simultaneously with next-to-leading-order fits to recent prompt photon and Drell-Yan data. As a result we are able to place tighter constraints on the quark and gluon distributions. Two definitive sets of parton distributions are presented according to whether the European Muon Collaboration or Bologna-CERN-Dubna-Munich-Saclay Collaboration muon data are included in the global fit. Comparisons with distributions obtained in earlier analyses are made and the consistency of data sets is investigated.

I. INTRODUCTION

Predictions for many important processes at hadron colliders depend on a reliable determination of the parton distributions. The accumulation of precision data over recent years now allows these distributions to be determined much more accurately than before. In particular high-statistics data are now available, and the next-to-leading-order QCD corrections are known, for the deep-inelastic lepton-nucleon scattering processes $\mu N \rightarrow \mu X$ and $\nu N \rightarrow \mu X$, for prompt photon production $pp \rightarrow \gamma X$, and for the Drell-Yan process $pN \rightarrow \mu^+ \mu^- X$. The various processes constrain different combinations of the parton density functions, and, when the data are analyzed together, a definitive set of parton distributions is obtained, as well as a measurement of Λ_{QCD} .

As far as the data are concerned, the situation has recently improved radically. First, a recent reanalysis¹ of the SLAC deep-inelastic scattering (DIS) data has shed new light on the disagreement between the European Muon Collaboration² (EMC) and Bologna-CERN-Dubna-Munich-Saclay (BCDMS)³ measurements of the proton structure function $F_2^{\mu p}$ obtained in deep-inelastic muon scattering. Second, improved measurements of the ratio $F_2^{\mu n}/F_2^{\mu p}$ have yielded consistent and much more accurate values than before.

In previous analyses of deep-inelastic lepton scattering data,⁴ we derived sets of parton distributions which we denoted E and B, respectively, and, in a subsequent analysis,⁵ we refined these distributions by including data on prompt photon production and the Drell-Yan process.

The main features of the present analysis are that (i) the improved understanding of the deep-inelastic structure functions reduces the uncertainty in the determination of the quark distributions, and (ii) incorporating the prompt photon production and Drell-Yan process data in a systematic way tightly constrains the gluon and the

sea-quark distributions. In this way, we arrive at sets of parton distributions which are pinned down much more precisely than hitherto. Compared with previous analyses, the resulting parton distributions represent a reasonably definitive set which accurately reproduce a wide range of data. As a consequence, many quantities, such as W , Z , jet, and heavy-quark production at present and future hadron colliders, can now be predicted with greater certainty.

II. DATA USED IN THE ANALYSIS

For $F_2^{\mu p}$ we use the EMC² and BCDMS³ measurements. As is well known, there is a serious disagreement between the two data sets, as shown in Fig. 1. At small x , we see that the BCDMS data are some 10–15% higher.

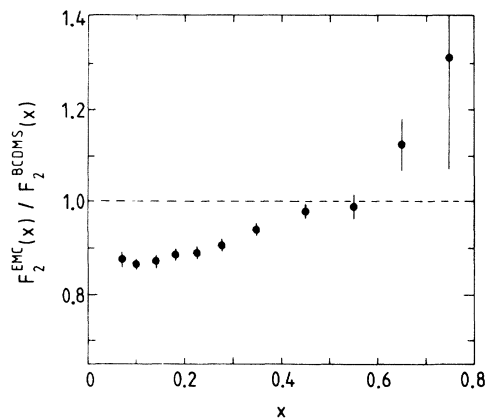


FIG. 1. The (Q^2 -averaged) ratio of the $F_2^{\mu p}$ structure functions measured by EMC (Ref. 2) and BCDMS (Ref. 3).

Because of this, it has not been possible to extract a unique set of parton distributions consistent with both experiments. However, a recent reanalysis of the earlier SLAC deep-inelastic electron scattering data extends their previous kinematic range to higher Q^2 , and into the region of overlap with the muon scattering data. Consistency between the EMC and SLAC data sets can be achieved over the whole x range by renormalizing the EMC data upwards by about 8%. Such a rescaling of the EMC data is also supported (i) by previous attempts⁴ to perform a combined analysis of muon and neutrino data which required a relative rescaling of one of the data sets by about 10% and (ii) by the overlap of their new low- x , low- Q^2 $F_2^{\mu D}$ data⁶ with their earlier high- Q^2 measurements.

A comparison of the BCDMS and SLAC data is a little more subtle. The overall normalization is more satisfactory; in fact there is excellent agreement in the mid- x range. At small x there is some indication that the BCDMS data need to be decreased by a few percent. Such a shift would be within the quoted BCDMS normalization uncertainty.³ At large x the BCDMS data appear to be systematically lower than the SLAC data in the Q^2 -overlap region. However, the high- x , low- Q^2 BCDMS data have sizable systematic uncertainties from the magnetic field and beam calibrations.⁷ Fortunately, it is precisely this kinematic region that is removed by the cuts that we impose to minimize the effects of higher-twist processes (i.e., $W^2 > 10 \text{ GeV}^2$, $Q^2 > 5 \text{ GeV}^2$). (Note that these cuts are in addition to those imposed in Ref. 3.)

Using the SLAC data normalization as a base, we perform a global renormalization of the EMC and BCDMS data of +8% and -2%, respectively. The effect of the renormalization is to reduce the discrepancy between the EMC and BCDMS $F_2^{\mu p}$ data at low x , but the two data sets are still mutually inconsistent: the basic difference in the shape of the structure function is now manifested as a serious discrepancy at large x . We cannot, therefore, combine these data but have to perform the analysis using each $F_2^{\mu p}$ data set in turn. Each of the two $F_2^{\mu p}$ data sets is supplemented by the measurements of $F_2^{\mu n}/F_2^{\mu p}$ made by EMC,⁸ BCDMS,⁹ and the New Muon Collaboration (NMC).¹⁰ We denote these two deep-inelastic $\mu N \rightarrow \mu X$ data sets by $\text{DIS}(\mu)_E$ and $\text{DIS}(\mu)_B$, where the subscript indicates the origin of the $F_2^{\mu p}$ data.

For deep-inelastic neutrino scattering, we use the high-statistics measurements of F_2 and xF_3 obtained by the CERN-Dortmund-Heidelberg-Saclay-Warsaw (CDHSW) Collaboration,¹¹ with the nuclear structure functions corrected for the EMC effect. We assume that xF_3 is corrected in the same way as F_2 . We denote these data by $\text{DIS}(\nu)$.

We use the prompt photon (PP) data of the CERN WA70 Collaboration¹² as representative of the photon transverse-momentum (p_T) distribution in the process $pp \rightarrow \gamma X$. Finally, for the Drell-Yan (DY) process, $pN \rightarrow \mu^+ \mu^- X$, we fit to the cross section $s d^2\sigma/d\sqrt{\tau} dy$ measured recently by the Fermilab E605 Collaboration.¹³ Data for these two processes give rather direct information on the gluon and sea-quark distributions, respectively, via the dominant QCD subprocesses $qg \rightarrow \gamma q$ and

$q\bar{q} \rightarrow \gamma^*$.

We fit to all the above data sets using the appropriate next-to-leading-order QCD formulas. All these higher-order calculations are performed in the modified minimal-subtraction ($\overline{\text{MS}}$) renormalization scheme and so Λ_{QCD} denotes $\Lambda_{\overline{\text{MS}}}$ (with four flavors). The quark distributions are defined in the universal $\overline{\text{MS}}$ factorization scheme. The following parametrization is used to describe the parton distributions of the proton at $Q^2 = Q_0^2 = 4 \text{ GeV}^2$:

$$x(u_V + d_V) = N_{ud} x^{\eta_1} (1-x)^{\eta_2} (1 + \gamma_{ud} x), \quad (1)$$

$$x d_V = N_d x^{\eta_3} (1-x)^{\eta_4} (1 + \gamma_d x), \quad (2)$$

$$2x(\bar{u} + \bar{d} + \bar{s}) = A_s x^{\delta_s} (1-x)^{\eta_s}, \quad (3)$$

$$xg = A_g (1-x)^{\eta_g}, \quad (4)$$

where, in the valence-quark distributions q_V , the coefficients N_q are fixed in terms of the appropriate η_i 's and γ_q 's so as to reproduce the flavor content of the proton. At $Q^2 = Q_0^2$ we assume

$$\bar{u} = \bar{d} = 2\bar{s},$$

where the fraction of the strange sea is chosen so as to reproduce the observed ratio of neutrino-induced dimuon ($\mu^+ \mu^-$) to single-muon events.¹⁴ [We repeated the analysis with an SU(3)-symmetric sea ($\bar{u} = \bar{d} = \bar{s}$) and found little sensitivity to the assumption that is made for the sea.] The charm distribution is generated through the evolution equations assuming that the charm quark is massless and that $c(x, Q_0^2) = 0$. This procedure has been shown¹⁵ to give a good description of the measured charm structure function $F_2^{c\bar{c}}$.¹⁶ We compare the behavior of the sea-quark distributions, including the heavy flavor distributions $c(x, Q^2)$ and $b(x, Q^2)$, in Sec. V. The coefficient A_g of the gluon distribution is determined by the momentum sum rule and so, including $\Lambda_{\overline{\text{MS}}}$, there is a total of 11 free parameters to be determined by the data.

III. COMBINED FIT TO THE DEEP-INELASTIC SCATTERING DATA AND PROMPT PHOTON DATA

As is well known, the deep-inelastic data on their own do not determine the gluon distribution very well. Large variations of $g(x, Q^2)$ can be compensated by small variations of the quark distributions and of $\Lambda_{\overline{\text{MS}}}$, viz., larger η_g (a softer gluon) correlates with smaller $\Lambda_{\overline{\text{MS}}}$. Although the gluon is not well constrained by deep-inelastic lepton scattering data, these data *do* determine the quark distributions.

The ambiguity in the form of the gluon distribution is considerably reduced if data on prompt photon production are included in the fits.¹⁷ In the description of the process $pp \rightarrow \gamma X$ (unlike that of deep-inelastic lepton scattering), the gluon enters directly at leading order via the dominant QCD subprocess $gq \rightarrow \gamma q$. Data for the process $pp \rightarrow \gamma X$, therefore, provide a direct measure of the gluon distribution.

To construct the χ^2 contour plots shown in Figs. 2(a)–2(d), we first perform fits to all the deep-inelastic

scattering data for different fixed values of $\Lambda_{\overline{\text{MS}}}$ and η_g , and produce an optimal set of parton distributions for each point in the η_g - $\Lambda_{\overline{\text{MS}}}$ plane. These parton distributions are then used to predict the prompt photon production cross section as a function of p_T . The calculation of the prompt photon cross section is performed beyond leading order using the principle of minimum sensitivity to determine the optimized factorization and renormalization scales as described in Ref. 18. Figures 2(a) and 2(b) show, in terms of contours of constant χ^2 , the quality

of the fit to the WA70 photon data¹² as a function of η_g and $\Lambda_{\overline{\text{MS}}}$. These data clearly favor a value of η_g in the region $4 \lesssim \eta_g \lesssim 5$, but do not constrain $\Lambda_{\overline{\text{MS}}}$ very strongly. However, if we combine these χ^2 values (giving the quality of the description of the prompt photon data) with those obtained in the original fits to the DIS(μ) + DIS(ν) data then we obtain the contour plots shown in Figs. 2(c) and 2(d) and we see that $\Lambda_{\overline{\text{MS}}}$ is better determined. The values of η_g and $\Lambda_{\overline{\text{MS}}}$ at the minimum value of χ^2 are

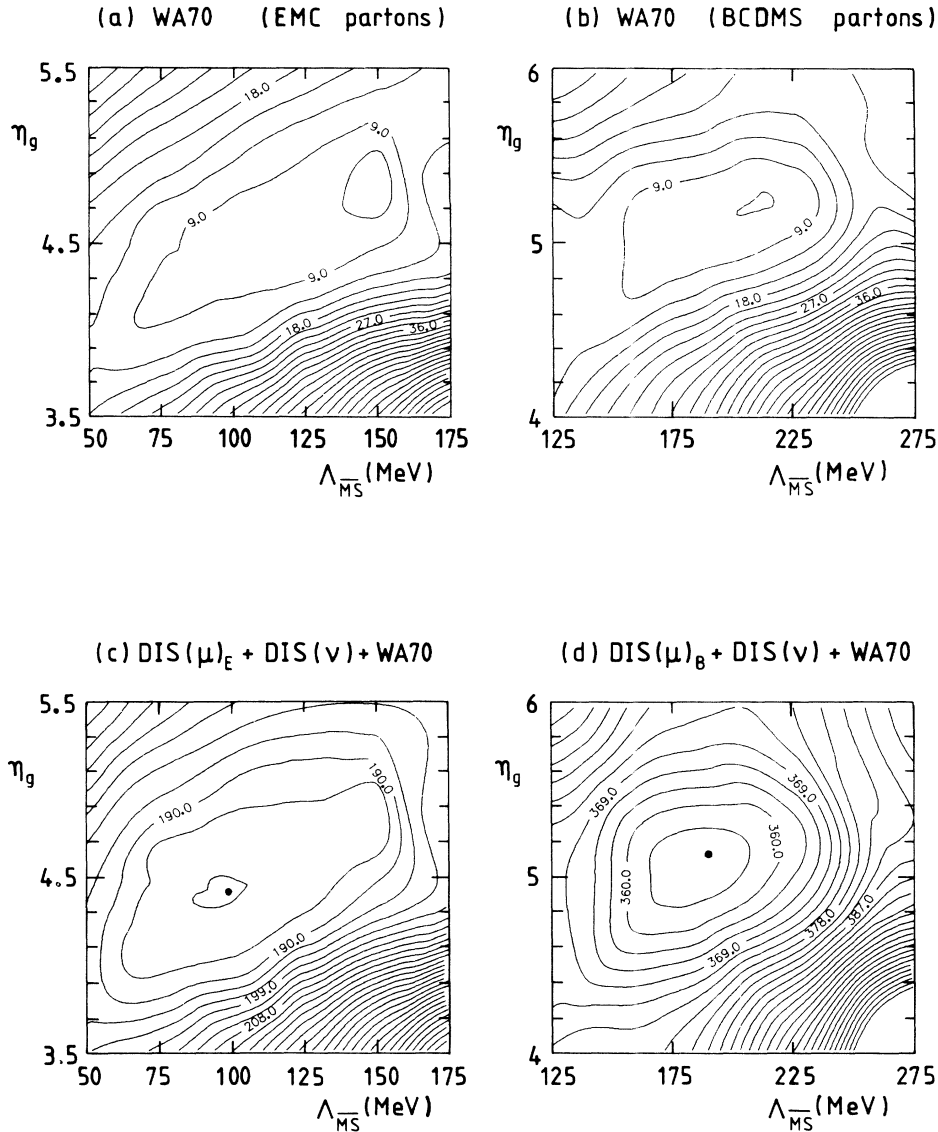


FIG. 2. (a) and (b) show contours of constant χ^2 (with 3 unit spacing) in the η_g - $\Lambda_{\overline{\text{MS}}}$ plane, where χ^2 simply measures the quality of the prediction for the WA70 prompt photon data by the various sets of parton distributions obtained in fitting to the DIS(μ) + DIS(ν) data, incorporating (a) EMC or (b) BCDMS $F_2^{\mu p}$ measurements. The statistical and systematic errors on the WA70 data have been combined in quadrature. The χ^2 contour plots (c) and (d) show the quality of the *simultaneous* description of the DIS(μ) + DIS(ν) and prompt photon data. The optimum overall description is obtained for the values of η_g and $\Lambda_{\overline{\text{MS}}}$ shown as the solid dots in (c) and (d); the columns denoted by A in Table I list the corresponding values of the parameters and the contributions to the total χ^2 from the various data sets.

$$\eta_g = 4.4, \quad \Lambda_{\overline{\text{MS}}} = 100 \pm 20 \text{ MeV}$$

$$[\text{DIS}(\mu)_E + \text{DIS}(\nu) + \text{prompt photon}], \quad (5)$$

$$\eta_g = 5.1, \quad \Lambda_{\overline{\text{MS}}} = 190 \pm 20 \text{ MeV}$$

$$[\text{DIS}(\mu)_B + \text{DIS}(\nu) + \text{prompt photon}],$$

where the errors on the $\Lambda_{\overline{\text{MS}}}$ values represent the change which corresponds to an increase in χ^2 of approximately one unit from the minimum value. The details of these optimum fits are listed in Table I in the columns marked A.

IV. INCLUSION OF DRELL-YAN DATA

Next, we study the constraints that are imposed on the parton distributions by Drell-Yan data. The cross section for producing a $\mu^+\mu^-$ pair of invariant mass M and rapidity y in pp collisions of energy \sqrt{s} is

$$\frac{d^2\sigma}{dM dy} = \frac{8\pi\alpha^2}{9Ms} K(y, M^2) \times \left[\sum_q e_q^2 q(x_1, M^2) \bar{q}(x_2, M^2) + (q \leftrightarrow \bar{q}) \right], \quad (6)$$

where $x_{1,2} = \sqrt{\tau} e^{\pm y}$ with $\sqrt{\tau} = M/\sqrt{s}$. The form of this cross section shows that the dimuon distribution is

TABLE I. In the upper portion of the table, we list the parameter values of the parton distributions and, in the lower portion, the contributions to the total χ^2 arising from the individual data sets of the optimum fits described in the text. The fits corresponding to the two columns denoted by A do not include the Drell-Yan data; the χ^2 values shown in brackets are obtained by taking $K'_{\text{opt}} = 1.06$ and 0.96 for EMC and BCDMS, respectively. For convenience, we also list the values of N_{ud} , N_d , and A_g which are determined by the 11 parameters of the fit and the percentage of the proton's total momentum carried by each type of parton at $Q^2 = Q_0^2 = 4 \text{ GeV}^2$. Our final optimum HMRS(E) and HMRS(B) parton distributions correspond to the two columns denoted by B, and the description of the data is shown, respectively, by the continuous and dashed curves in Figs. 5–10. PP denotes prompt photon.

	With EMC		With BCDMS		
	+PP A	+DY B	+PP A	+DY B	
η_g	4.4	4.4	5.1	5.1	
$\Lambda_{\overline{\text{MS}}}$	100	100	190	190	
η_1	0.357	0.352	0.224	0.237	
η_2	4.07	4.08	4.06	4.07	
γ_{ud}	10.0	10.6	26.6	23.8	
η_3	0.608	0.607	0.411	0.426	
η_4	4.82	4.83	4.81	4.82	
γ_d	1.13	1.26	7.05	6.32	
A_S	3.22	4.50	5.35	5.25	
δ_S	0.270	0.359	0.404	0.401	
η_S	9.45	10.5	9.87	9.75	
N_{ud}	1.264	1.216	0.4893	0.5469	
N_d	1.754	1.735	0.6384	0.6957	
A_g	2.614	2.622	2.856	2.855	
$P(u_V)$	26.4%	26.5%	26.2%	26.2%	
$P(d_V)$	10.6%	10.7%	10.7%	10.7%	
$P(S)$	14.5%	14.2%	16.2%	16.3%	
$P(g)$	48.4%	48.5%	46.8%	46.8%	
Data	No. of points		χ^2 values		
$F_2^{\mu p}$ (EMC,BCDMS)	[88,142]	58.1	58.6	163.8	163.8
F_2^{ν} (CDHSW)	[84]	27.0	25.8	52.9	54.6
$x F_3^{\nu}$ (CDHSW)	[94]	71.3	73.0	116.3	115.4
$F_2^{\mu n} / F_2^{\mu p}$ (BCDMS)	[11]	5.9	6.2	9.2	8.7
$F_2^{\mu n} / F_2^{\mu p}$ (EMC)	[10]	4.1	4.1	2.9	2.8
$F_2^{\mu n} / F_2^{\mu p}$ (NMC)	[11]	10.3	10.6	4.3	4.1
DIS (total)	[298,352]	176.7	178.3	349.3	349.3
Prompt photon (WA70)	[8]	7.2	7.2	7.3	7.3
Drell-Yan (E605)	[8]	(19.2)	12.4	(12.0)	11.8
Total	[314,368]	203.1	197.9	368.6	368.4

directly sensitive to the shape of the sea distribution q_S . We may write $K = K_0 K'$, where $K_0(y, M^2)$ is a known function which arises from the first-order QCD corrections to the subprocess $q\bar{q} \rightarrow \gamma^*$ and $K'(y, M^2)$ allows for the effect of second- and higher-order corrections. The mean value of K_0 for the kinematic region of the E605 Drell-Yan data is found to be 1.51 and 1.62 using the parton distributions which gave the optimum overall description of the $\text{DIS}(\mu) + \text{DIS}(\nu)$ and prompt photon data. The two values correspond to the inclusion of either the EMC or BCDMS muon data, respectively. K_0 increases gradually with $\sqrt{\tau}$. Since the first-order corrections are of the order of 50%, it is necessary to allow K' to be a (constant) parameter to be determined by the Drell-Yan data.

We proceed as follows. First we fix η_g and $\Lambda_{\overline{\text{MS}}}$ according to Eq. (5) and repeat the fits to the

$\text{DIS}(\mu) + \text{DIS}(\nu)$ data for different fixed values of A_S and η_S . This enables us to predict the cross section for the Drell-Yan process for a range of possible sea-quark distributions which vary in shape and magnitude. Each set of parton distributions can then be used to calculate the E605 Drell-Yan distribution and hence to determine a value of $K' = K'_{\text{opt}}$ which minimizes the χ^2 arising from the E605 data. Figures 3 and 4 display the results of this analysis in the $\eta_S - A_S$ plane according as to whether we include the EMC or BCDMS muon data. In each case the overall optimum fit is shown by a solid dot in Figs. 3(d) and 4(d) and corresponds to the values

$$\begin{aligned} A_S = 4.5, \quad \eta_S = 10.5, \quad K' = 1.15 \quad (\text{EMC}), \\ A_S = 5.25, \quad \eta_S = 9.75, \quad K' = 0.94 \quad (\text{BCDMS}). \end{aligned} \quad (7)$$

The χ^2 contours shown in Figs. 3(d) and 4(d) are the sum

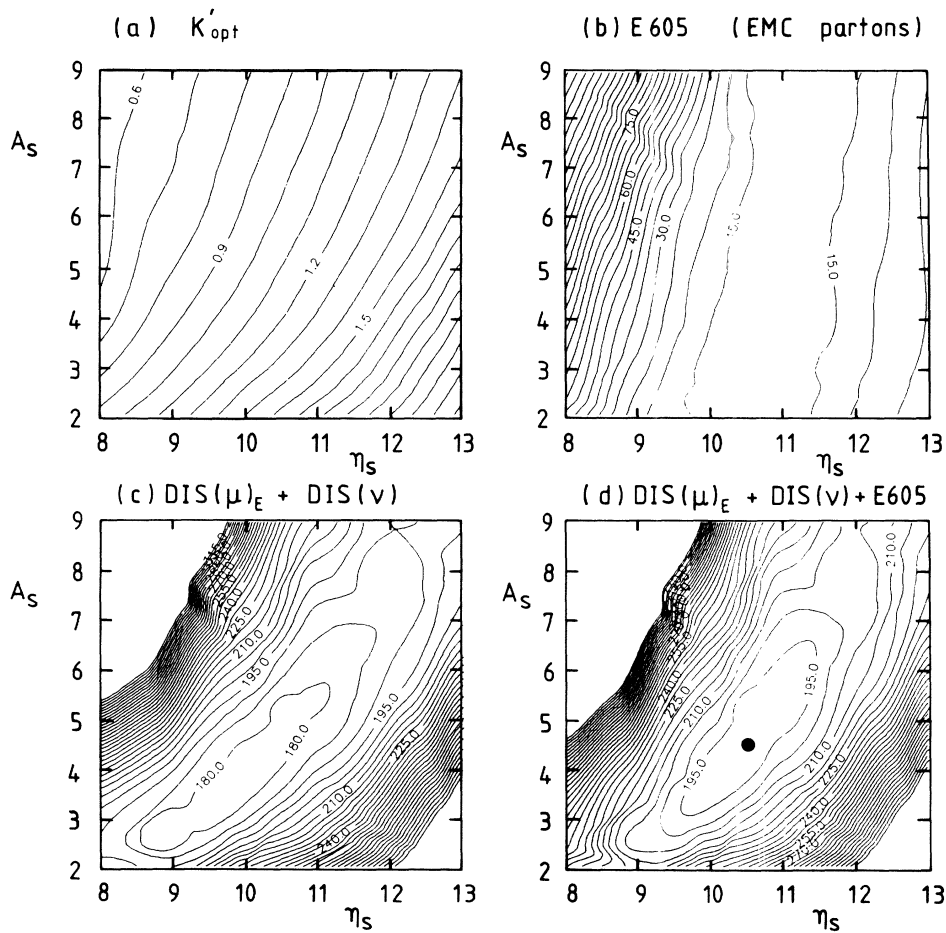


FIG. 3. The improvement in the determination of the parameters η_S , A_S of the sea distribution on including the E605 Drell-Yan data (Ref. 13). (c) shows the χ^2 contours in the $\eta_S - A_S$ plane obtained in fits to DIS data which include the EMC $F_2^{\mu p}$ measurements. (b) shows the χ^2 contours for the corresponding description of the E605 Drell-Yan data, optimized by varying K' ; (a) the optimum values of K' . (d) shows the combined χ^2 contours with the optimum overall fit shown as a solid dot corresponding to the HMRS(E) parton distributions which are detailed in the first column denoted by B in Table I.

of the χ^2 contours for the E605 Drell-Yan data [Figs. 3(b) and 4(b)] and for the deep-inelastic lepton data [Figs. 3(c) and 4(c)]. As may be expected, the inclusion of the Drell-Yan data improves the determination of η_S . For completeness we show in Figs. 3(a) and 4(a) the values of K'_{opt} as a function of η_S and A_S . The values corresponding to the optimum overall fit are given in Eqs. (7). It is reassuring that these values found for K' are approximately unity and not unreasonable for the size of second- and higher-order QCD corrections.

The details of the overall optimum fits and the accompanying parton distributions are listed in Table I in the columns denoted by B. We denote these distributions by HMRS(E) and HMRS(B), corresponding to the EMC and BCDMS data sets, respectively. We see from Table I that in fact the distributions are changed very little by the inclusion of the Drell-Yan data. This is particularly so for the HMRS(B) fit, where the deep-inelastic and prompt photon fit already gives an excellent description of the Drell-Yan data. We can regard this as an excellent

overall consistency check on the data from the various processes.

The continuous and dashed curves in Figs. 5–10 show the description of the data by the HMRS(E) and HMRS(B) sets of parton distributions, respectively. The overall description of the data is excellent in both cases. From Figs. 6, 7, and 8 we see that the BCDMS data appear to be somewhat less compatible with the neutrino data than the EMC data. This is also evident from the χ^2 values shown in Table I. However, care must be taken in concluding that this favors the EMC, rather than the BCDMS, shape of $F_2^{\mu p}$, particularly because of the higher precision of the latter data and the constraints imposed by our parametrizations. Nevertheless, in Sec. VI we shall reexamine the compatibility of the muon and neutrino data sets in a “model-independent” way. Another noteworthy feature is the increased precision of the new NMC data for $F_2^{\mu n}/F_2^{\mu p}$, which is well described in both fits. This has important implications for precision measurements in W and Z production at $p\bar{p}$ colliders²⁰ (see

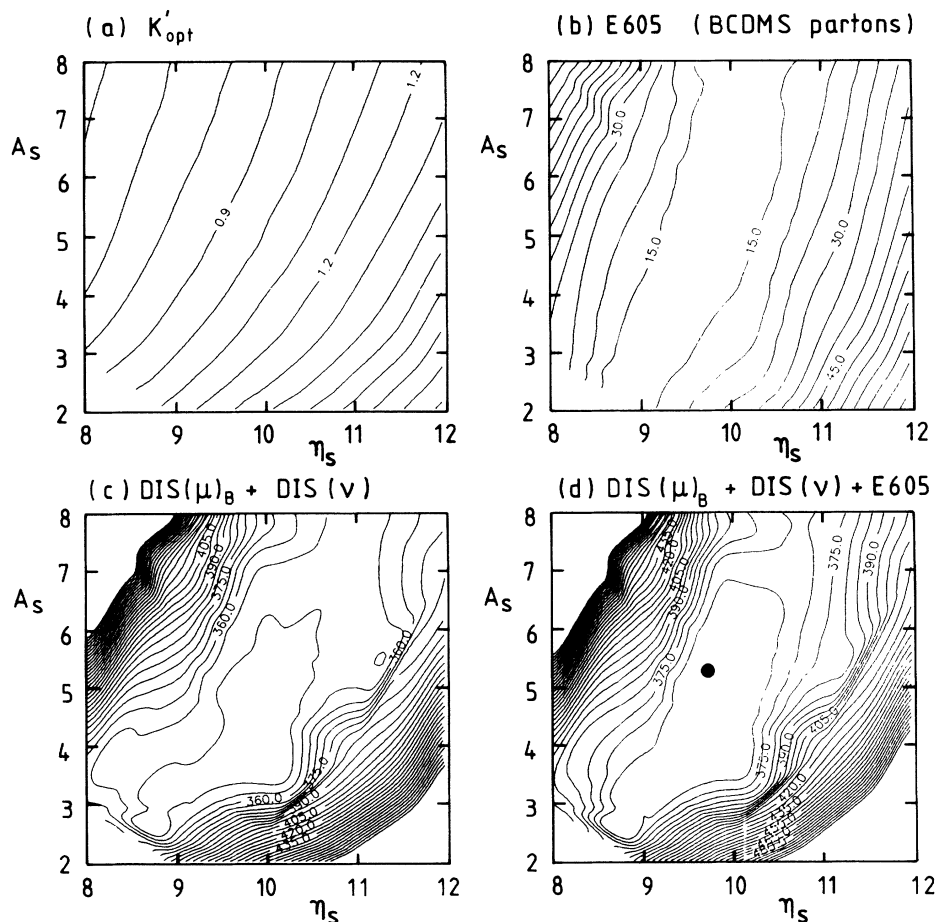


FIG. 4. As for Fig. 3, but with the EMC $F_2^{\mu p}$ data replaced by the BCDMS $F_2^{\mu p}$ measurements. The dot in (d) corresponds to the HMRS(B) parton distributions detailed in the last column of Table I.

below). In Sec. VI we examine how well earlier sets of parton distributions describe these new data.

V. PARTON DISTRIBUTIONS

We have determined the parton distributions of the proton using high-statistics data on deep-inelastic muon and neutrino scattering, together with that on prompt photon production and the Drell-Yan process in high-

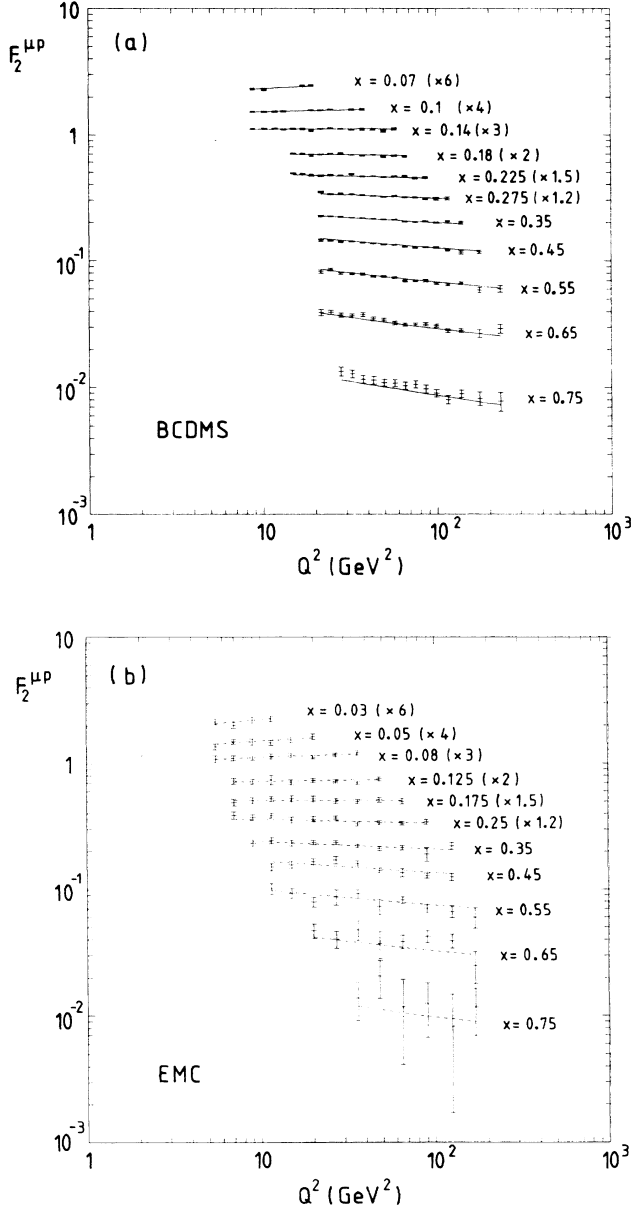


FIG. 5. Data on the structure function $F_2^{\mu p}(x, Q^2)$ from (a) the BCDMS Collaboration (Ref. 3) and (b) the EM Collaboration (Ref. 2) together with, respectively, the HMRS(B) (continuous lines) and HMRS(E) (dashed lines) fits. The BCDMS and EMC data are renormalized by -2% and $+8\%$, respectively, as discussed in the text.

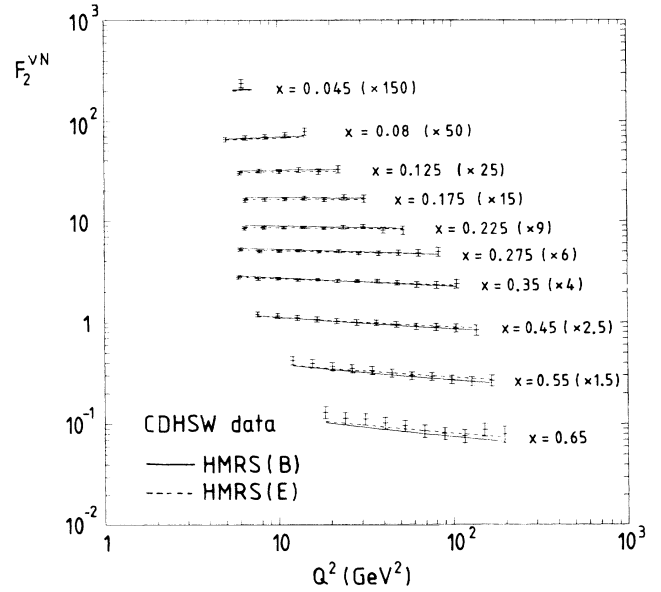


FIG. 6. Data on the structure function $F_2^{vN}(x, Q^2)$ from the CDHSW Collaboration (Ref. 11), together with the HMRS(B) (continuous lines) and HMRS(E) (dashed lines) fits. The data have been corrected for the “EMC effect.”

energy proton-proton collisions. Data on all four of these processes are in principle necessary to obtain definitive parton distributions. By performing fits to each data set separately, we have also explored which set most constrains each parton distribution. Our findings are sum-

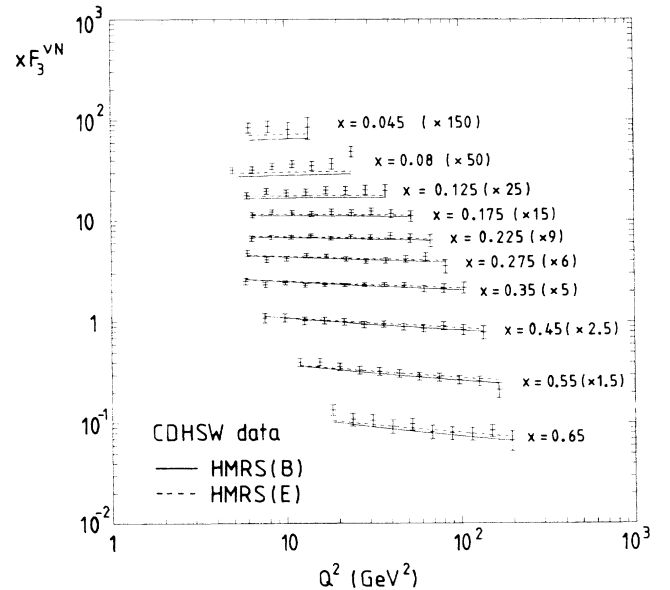


FIG. 7. Data on the structure function $xF_3^{vN}(x, Q^2)$ from the CDHSW Collaboration (Ref. 11), together with the HMRS(B) (continuous lines) and HMRS(E) (dashed lines) fits. The data have been corrected for the “EMC effect.”

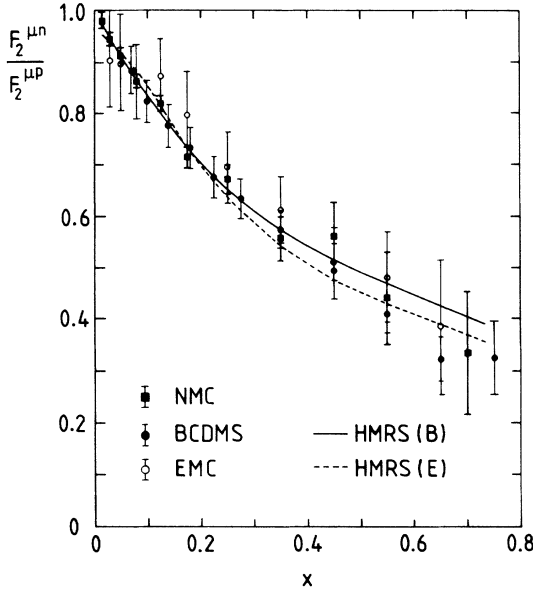


FIG. 8. Data on the structure function ratio F_2^{nn}/F_2^{pp} from the EM Collaboration (Ref. 8) (open circles), the BCDMS Collaboration (Ref. 9) (closed circles), and the NM Collaboration (Ref. 10) (solid squares), together with the HMRS(B) (continuous line) and HMRS(E) (dashed line) fits.

marized in Table I. As a consequence of the correlation between η_g and $\Lambda_{\overline{\text{MS}}}$, there is considerable ambiguity in the determination of $\Lambda_{\overline{\text{MS}}}$ by deep-inelastic data alone. Nevertheless, these data do determine the quark distributions.

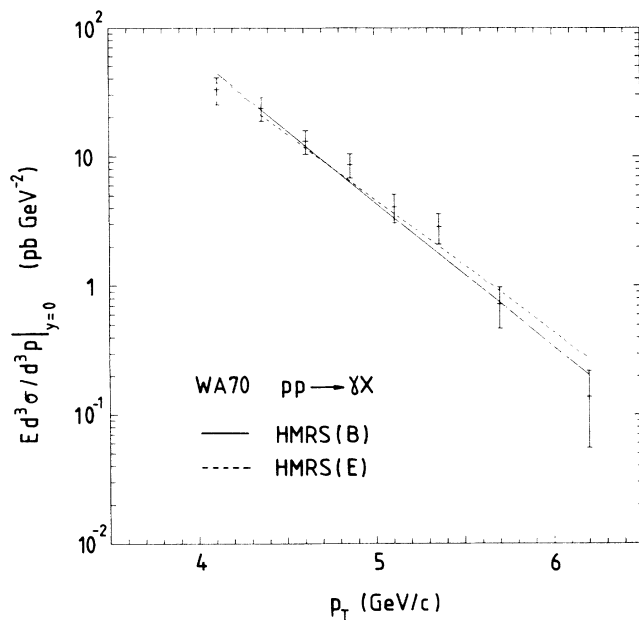


FIG. 9. Data on the prompt photon transverse-momentum distribution in pp collisions at $\sqrt{s}=23$ GeV from the WA70 Collaboration (Ref. 12) [corrected to $y=0$ (Ref. 19)], together with the predictions using the HMRS(B) (continuous line) and HMRS(E) (dashed line) parton distributions.

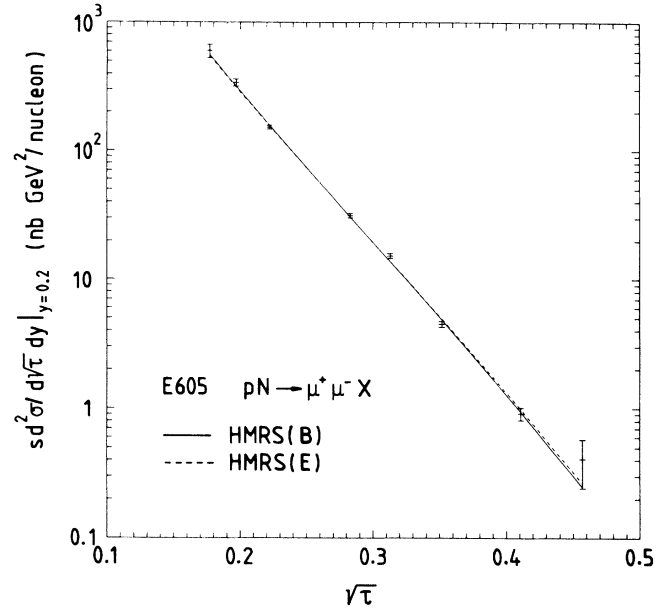


FIG. 10. Drell-Yan data from the E605 Collaboration (Ref. 13) in pN collisions at $\sqrt{s}=38.8$ GeV, together with the predictions using the HMRS(B) (continuous line) and HMRS(E) (dashed line) parton distributions.

COMPARISON OF PARTON DISTRIBUTIONS
AT $Q^2=20 \text{ GeV}^2$

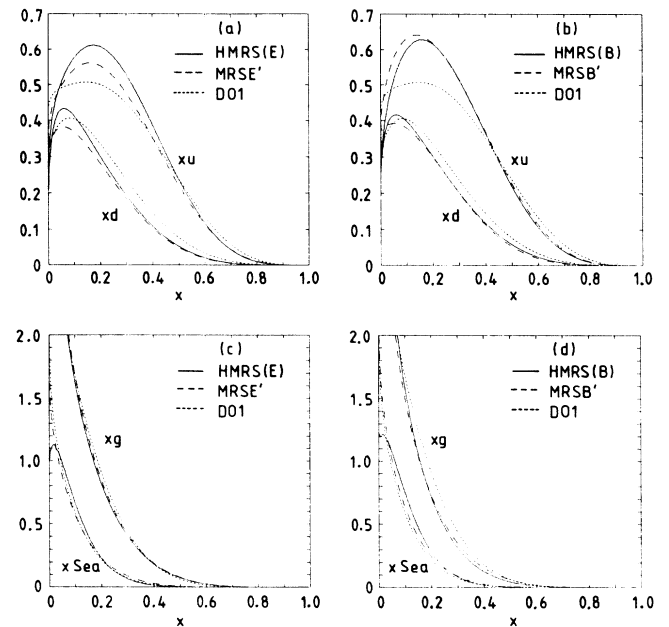


FIG. 11. The continuous and dashed curves are the HMRS and MRS' (Ref. 5) parton distributions $x f_i(x, Q^2=20 \text{ GeV}^2)$, respectively. The left- (right-)hand plots are the parton distributions obtained using data sets which include the EMC (BCDMS) F_2^{pp} measurements. In each case, we show the distributions of Duke and Owens (DO) set 1 (Ref. 21) for comparison.

The inclusion of data on prompt photon production is found to pin down the form of the gluon distribution and hence sharpen the determination of $\Lambda_{\overline{\text{MS}}}$. Equation (5) summarizes the resulting values of η_g and $\Lambda_{\overline{\text{MS}}}$. Finally, the incorporation of data on the Drell-Yan process is found to constrain tightly the form of the sea-quark distribution.

In Fig. 11, we compare our final distributions, HMRS(E) and HMRS(B), with our earlier MRSE' and MRSB' of Ref. 5, and, for reference, with set 1 of Duke and Owens.²¹ A comparison between the DO and HMRS distributions indicates that the former (particularly the valence quarks) are now in significant disagreement with the most recent deep-inelastic data. The differences between the HMRS and MRS' distributions are largely due to two factors: the renormalization of the respective $F_2^{\mu p}$ data sets and the inclusion of new, more precise $F_2^{\mu n}/F_2^{\mu p}$ data. The former gives the dominant effect at medium and large x while the latter influences the relative size of the valence and sea distributions at small x . The differences are magnified in the ratios of the different distributions. Thus Fig. 12 gives a comparison at $Q^2=20 \text{ GeV}^2$. Figure 12(a) shows the ratios $f_i(\text{HMRS(E)})/f_i(\text{MRSE}')$ and Fig. 12(b) shows $f_i(\text{HMRS(B)})/f_i(\text{MRSB}')$. For the fits that include the EMC data, we see that, compared with our earlier sets, u and d are increased by 5–10%. This is simply a

reflection of our upwards renormalization of the EMC data. Figures 12(c) and 12(d) show the difference between the E- and B-type parton distributions. Figure 12(c) is taken from Ref. 5 and Fig. 12(d) gives the ratios $f_i(\text{HMRS(B)})/f_i(\text{HMRS(E)})$ as obtained in this analysis in which the EMC data have been renormalized upwards by 8% and the BCDMS data downwards by 2%. Different starting assumptions have been made for the strength of the strange quarks in this analysis compared with our earlier analysis.⁵ The HMRS partons of this work have $\bar{u}=\bar{d}=2\bar{s}$ at $Q_0^2=4 \text{ GeV}^2$, whereas our previous MRSB' and MRSE' distributions were taken to satisfy $\bar{u}=\bar{d}=\bar{s}$ at $Q_0^2=4 \text{ GeV}^2$. Thus, in the comparisons of Figs. 11 and 12 we show

$$x \times \text{Sea} = 2x(\bar{u} + \bar{d} + \bar{s}).$$

In Fig. 13, we compare the individual sea-quark distributions together with that of the gluon, evolved to $Q^2=M_W^2$. The quark distributions of the heavy flavors are generated as $Q\bar{Q}$ via the gluon, assuming that $c(x, Q^2=4 \text{ GeV}^2)=0$ and $b(x, Q^2=100 \text{ GeV}^2)=0$. To implement this, we define nonsinglet quantities $f_i^{\text{NS}}(x, Q^2)$ for $i = \text{charm, bottom}$,

$$f_i^{\text{NS}}(x, Q^2) = N_f^{-1} F^{\text{S}}(x, Q^2) - [xq_i(x, Q^2) + x\bar{q}_i(x, Q^2)], \quad (8)$$

where $F^{\text{S}}(x, Q^2)$ is the flavor-singlet combination and N_f is the number of flavors appropriate to the value of Q^2 . The behavior of α_s across the bottom-quark threshold is chosen to match $\alpha_s(Q^2, N_f=4)$ with $\alpha_s(Q^2, N_f=5)$ at $4m_b^2 \approx 100 \text{ GeV}^2$, i.e., for $Q^2 > 4m_b^2$, the coupling α_s is given by

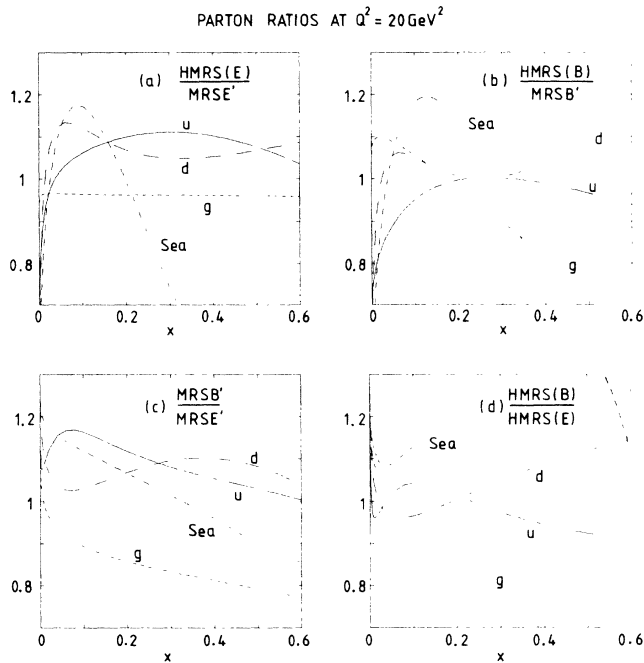


FIG. 12. Ratios of the quark and gluon distributions at $Q^2=20 \text{ GeV}^2$: (a) $f_i(\text{MRSE}')/f_i(\text{HMRS(E)})$; (b) $f_i(\text{MRSB}')/f_i(\text{HMRS(B)})$; (c) $f_i(\text{MRSB}')/f_i(\text{MRSE}')$; and (d) $f_i(\text{HMRS(B)})/f_i(\text{HMRS(E)})$.

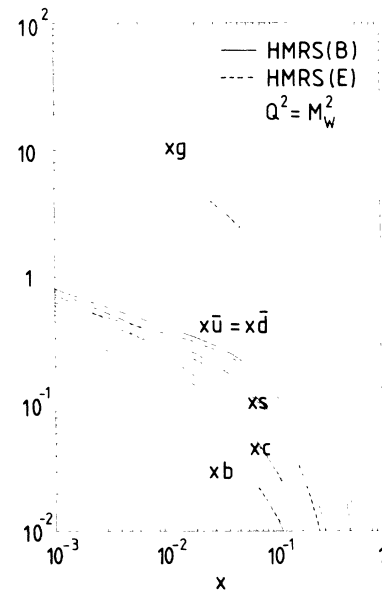


FIG. 13. The HMRS gluon and sea-quark distributions at $Q^2=M_W^2$.

TABLE II. Predictions for W and Z cross sections in $p\bar{p}$ collisions at $\sqrt{s}=630$ GeV and 1.8 TeV using the HMRS(B) and HMRS(E) distributions of the present study, and the MRSB' and MRSE' distributions from Ref. 5. The leptonic branching ratios $B_W \equiv B(W \rightarrow e\nu) = 0.109$ and $B_Z \equiv B(Z \rightarrow e^+e^-) = 0.0336$ are included. The values of the relevant parameters are taken to be $M_Z = 91.1$ GeV/ c^2 , $M_W = 80.0$ GeV/ c^2 , $\sin^2\theta_W = 0.229$, $m_t > M_W$, and $N_\nu = 3$. For comparison, we show the most recent UA2 (Ref. 22) and CDF (Ref. 23) measurements of these quantities.

$\sqrt{s} = 630$ GeV	$\sigma_W B_W$ (nb)	$\sigma_Z B_Z$ (nb)	$\frac{\sigma_W B_W}{\sigma_Z B_Z}$
HMRS(B)	0.705	0.0663	10.6
HMRS(E)	0.726	0.0676	10.7
MRSB'	0.683	0.0670	10.2
MRSE'	0.607	0.0579	10.5
UA2	$0.660 \pm 0.015 \pm 0.037$	$0.0704 \pm 0.0055 \pm 0.004$	$9.38^{+0.92}_{-0.72} \pm 0.25$
$\sqrt{s} = 1800$ GeV			
HMRS(B)	2.13	0.199	10.7
HMRS(E)	2.00	0.190	10.5
MRSB'	2.09	0.201	10.4
MRSE'	1.76	0.169	10.4
CDF	$2.06 \pm 0.04 \pm 0.13 \pm 0.31$	$0.197 \pm 0.012 \pm 0.01 \pm 0.03$	$10.45^{+0.9}_{-0.8}$

$$\alpha_s^{-1}(Q^2) = \alpha_s^{-1}(Q^2, N_f = 5) + \alpha_s^{-1}(4m_b^2, N_f = 4) - \alpha_s^{-1}(4m_b^2, N_f = 5). \quad (9)$$

The MRS' distributions have been widely distributed and used in a variety of phenomenological applications. Figure 12 shows that the updated distributions by and large represent a "fine tuning," and the effect on most cross-section predictions of replacing MRS' by HMRS distributions will be small. There is, however, one application— W and Z cross sections in $p\bar{p}$ collisions—where the level of experimental precision is sensitive to the differences between the old and new sets, and between the E- and B-type distributions. Table II shows the cross sections (times the leptonic branching ratios) for W and Z production at $\sqrt{s} = 630$ GeV and 1.8 TeV, for the HMRS(E) and HMRS(B) distributions, as compared to the predictions of the previous MRSE' and MRSB' distributions. The small differences can be completely understood by referring to the u and d ratios in Fig. 12. Thus, for example, at the CERN energy where $x \approx 0.15$, the change in the cross sections on going from the MRS' to the HMRS distributions simply reflects the rescaling of the $F_2^{\mu p}$ data sets. At the higher Fermilab energy, where $x \approx 0.05$, the differences are much less pronounced, consistent with the ratios in Fig. 12. The differences between the HMRS(B) and HMRS(E) predictions for the ratio R of W and Z cross sections are strongly correlated with the predictions for the $F_2^{\mu n}/F_2^{\mu p}$ ratio at the relevant x value. Although we see from Table II that the actual predictions for R have changed slightly from the values obtained using the MRS' distributions, the differences are still much less than the current experimental errors.^{22,23}

In Table III, we show the predictions for W and Z production at the $p\bar{p}$ supercollider energies of $\sqrt{s} = 16$ and 40 TeV. These results are sensitive to the sea-quark and gluon distributions at values of $x \approx M_W/\sqrt{s} \approx 0.005$ and less, which lie well below the lowest x values of the data

fitted in the structure-function analysis. It is, therefore, not surprising that the spread of the predictions shown in Table III exceeds those listed in Table II.

Although W and Z production through both qq and qg initiated processes have been included, at very high energies there may also be some contribution from gg initiated reactions. The determination of these gg reactions must await a calculation of the two-loop amplitudes. Moreover, at these supercollider energies, the x values probed can reach into the region $x \lesssim 10^{-4}$, where rescattering corrections could begin to be important.²⁴ For example, for W production at Superconducting Super Collider energies, 35% of the cross section corresponds to an incoming parton having $x < 10^{-4}$.

VI. CONCLUSIONS

In summary, our analysis has produced two sets of Q^2 -dependent parton distributions²⁵ which we claim are in advance of any previous set in that they have been forced to satisfy very tight constraints from a wide

TABLE III. As for Table II, but showing the predictions for W and Z cross sections in $p\bar{p}$ collisions at $\sqrt{s} = 16$ TeV and 40 TeV.

$\sqrt{s} = 16$ TeV	$\sigma_W B_W$ (nb)	$\sigma_Z B_Z$ (nb)	$\frac{\sigma_W B_W}{\sigma_Z B_Z}$
HMRS(B)	14.1	1.36	10.4
HMRS(E)	10.0	0.98	10.2
$\sqrt{s} = 40$ TeV			
HMRS(B)	31.3	3.09	10.1
HMRS(E)	20.7	2.07	10.0

variety of processes. The new measurements by NMC of $F_2^{\mu n}/F_2^{\mu p}$ are an example of the recent improvement in the precision of the data and the need to update the parton distributions. This is well illustrated by Fig. 14 which compares these data with the predictions obtained from other widely used parton distributions. It is clear that these data alone render the majority of earlier sets of parton distributions obsolete.

As with all fits of this type, it is important to remember that our final distributions constitute overall “best fits” to the data. We have not attempted the much harder task of obtaining a “band” of distributions designed to reflect the experimental errors on the data. Although all our fitted parameters do have associated errors, these are in general highly correlated and there is no straightforward systematic way of varying the parameters to derive “extreme” distributions.

In practice, however, one can in many cases gauge the allowed spread of the distributions by referring directly to the fits to the experimental data. As an example, the structure function $F_2^{\mu p}$ at large x is dominated by the u_V contribution, and the uncertainties in the former determine the allowed spread in the latter.

One of the *new* features has been the pinning down of the normalization of the muon DIS data from the re-

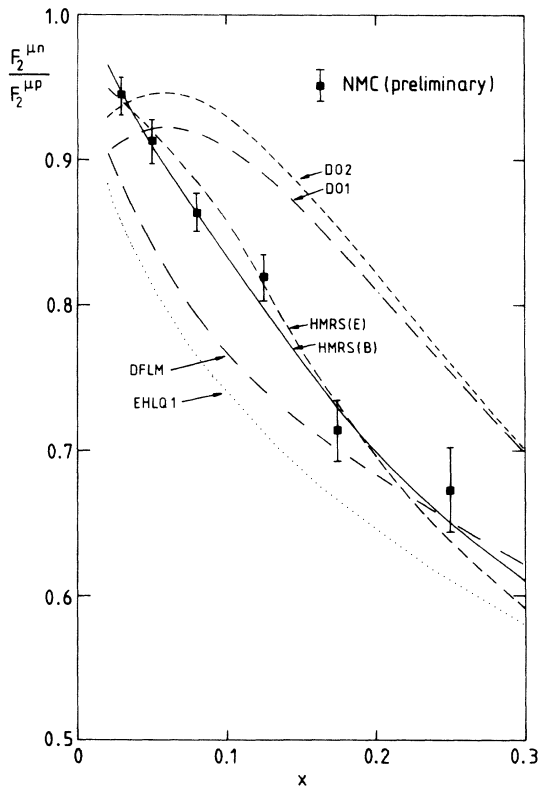


FIG. 14. Comparison of the predictions for the ratio $F_2^{\mu n}/F_2^{\mu p}$ using various parton distributions [HMRS(E), HMRS(B), DO1, DO2 (Ref. 21), Eichten-Hinchliffe-Lane-Quigg set (Ref. 26) and Diemoz-Ferroni-Longo-Martinelli (Ref. 27)] with data from the NMC Collaboration (Ref. 10) (solid squares).

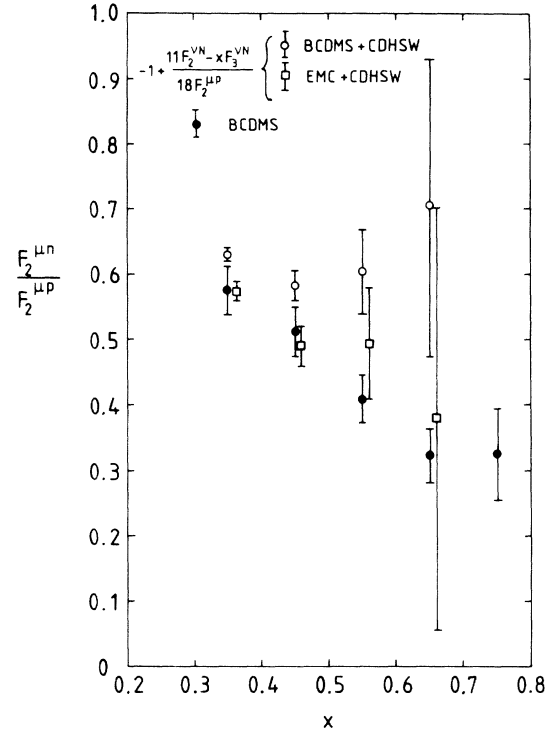


FIG. 15. Comparison of large- x $F_2^{\mu n}/F_2^{\mu p}$ data from the BCDMS Collaboration (Ref. 9) (solid circles) with the “effective” ratio derived from the F_2 and xF_3 structure-function data [according to Eq. (10)], using, respectively, the EMC (open squares) and BCDMS (open circles) $F_2^{\mu p}$ data. Note that the neutrino data are corrected for the “EMC effect.”

quirement of consistency with the reanalyzed SLAC data at lower Q^2 . As we have noted, this has resulted in a reduction of the discrepancy between the two-muon DIS data sets, from EMC and BCDMS, at least at small x . Of course, the ultimate goal in an analysis of this kind is to end up with a *single* “unique” set of parton distributions which are consistent with all known correct data on processes which involve the distributions. With this aim in mind, it is reasonable to ask if one can remove the final obstacle to this goal by discriminating against one of the mutually inconsistent data sets—at least in the region where there is a conflict.

The x dependence of the $F_2^{\mu n}/F_2^{\mu p}$ ratio has recently become much more precisely determined. We can attempt to use these measurements as a criterion for checking the consistency of each of the $F_2^{\mu p}$ data sets at large x if we appeal to data on $F_2^{\nu N}$ and $xF_3^{\nu N}$ as an independent source of extra information. Thus, assuming $\bar{u} = \bar{d} = 2\bar{s}$, we have

$$\frac{F_2^{\mu n}}{F_2^{\mu p}} = -1 + \frac{11F_2^{\nu N} - xF_3^{\nu N}}{18F_2^{\mu p}} \quad (10)$$

or with similar expressions corresponding to different flavor assumptions about the sea. (The differences are negligible in the region of interest: $x \gtrsim 0.3$.) Figure 15 shows this comparison using, respectively, the EMC and

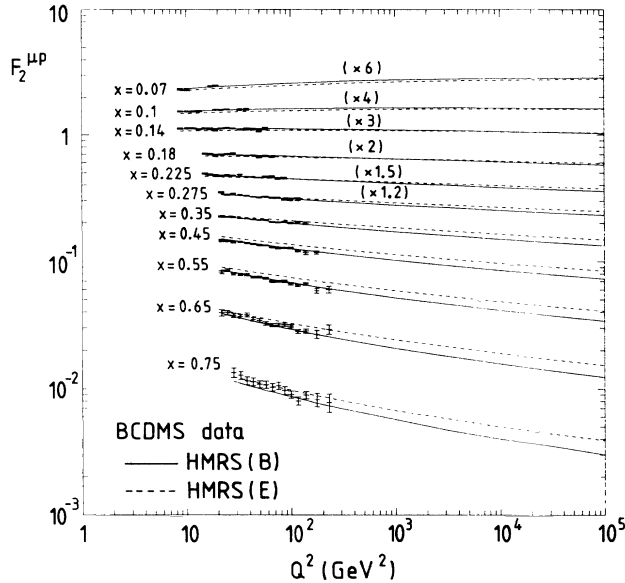


FIG. 16. Predictions for $F_2^{\mu p}(x, Q^2)$ (electromagnetic part only) extrapolated to the HERA kinematic region. The data are from the BCDMS Collaboration (Ref. 3) and the dashed and continuous curves correspond to the HMRS(E) and HMRS(B) parton distributions, respectively.

BCDMS $F_2^{\mu p}$ data combined with the neutrino data. An interpretation of this exercise would appear to be that it is the BCDMS data which are somewhat “out of line” at large x . Thus the price to pay for achieving a single consistent set of parton distributions would seem to be a readjustment of the large- x BCDMS $F_2^{\mu p}$ data.

Within a few years the DESY ep collider HERA will begin to make measurements of deep-inelastic structure functions at very high Q^2 ($\sim 10^4$ GeV 2). Our parametrizations provide the most accurate benchmark predictions for HERA. Thus Figs. 16 and 17 show the predictions for $F_2(x, Q^2)$ (electromagnetic part only) extrapolated to the appropriate kinematic region. [Note that Z^0 exchange contributes to the neutral-current cross section when $Q^2/(Q^2 + M_Z^2) \gtrsim 1$ —this is illustrated by the dashed-dotted line in Fig. 17.] The solid and dashed lines correspond to the HMRS(E) and HMRS(B) parton distributions, respectively. Notice that the differences in the F_2 predictions, discussed earlier in this paper, persist at higher Q^2 . Also evident is the dispersion in the predic-

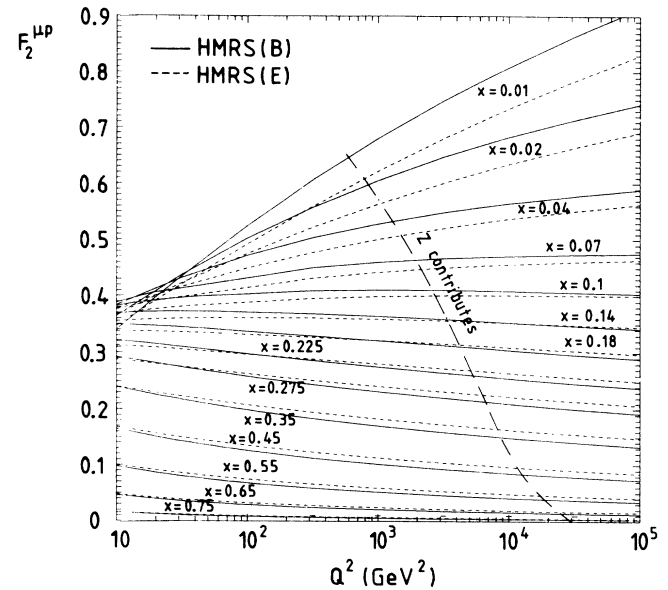


FIG. 17. As for Fig. 16 but with a linear scale for the structure function. The kinematic region where Z^0 exchange becomes important is indicated by the dashed-dotted line.

tions arising from the different $\Lambda_{\overline{\text{MS}}}$ values of the two fits. Blümlein *et al.* have performed detailed simulations of structure functions at HERA.^{28,29} It turns out that F_2 can be measured up to a maximum Q^2 which corresponds roughly to the region where Z exchange becomes important.²⁹ A comparison of Fig. 17 with Fig. 3 of Ref. 29 shows that it should be possible to discriminate between the two predictions for F_2 in the x range: $0.01 \lesssim x \lesssim 0.5$, and so HERA should be able to resolve the apparent discrepancy in the shape of the F_2 structure function as measured by EMC and BCDMS.

ACKNOWLEDGMENTS

We would like to thank Patrick Aurenche for providing us with his prompt photon program, and also Chuck Brown, Alain Milsztajn, and Marc Virchaux, Jan Nassalski, Peter Norton, and Terry Sloan, and Bert Turnbull for helpful discussions regarding the E605, BCDMS, NMC, EMC, and WA70 data, respectively. One of us (P.N.H.) thanks Durham University for financial support.

¹L. W. Whitlow *et al.*, Report No. SLAC-PUB-5100, 1989 (unpublished).

²EMC, J. J. Aubert *et al.*, Nucl. Phys. **B259**, 189 (1985).

³BCDMS Collaboration, A. C. Benvenuti *et al.*, Phys. Lett. B **223**, 485 (1989).

⁴A. D. Martin, R. G. Roberts, and W. J. Stirling, Phys. Lett. B **206**, 327 (1988).

⁵A. D. Martin, R. G. Roberts, and W. J. Stirling, Mod. Phys. Lett. A **4**, 1135 (1989).

⁶EMC, M. Arneodo *et al.*, Nucl. Phys. **B333**, 1 (1990).

⁷BCDMS Collaboration, A. Milsztajn (private communication).

⁸EMC, J. J. Aubert *et al.*, Nucl. Phys. **B293**, 740 (1987).

⁹BCDMS Collaboration, A. C. Benvenuti *et al.*, Phys. Lett. B **237**, 599 (1990).

¹⁰NMC, J. Nassalski, in Proceedings of the Europhysics Conference on High Energy Physics, Madrid, Spain, 1989 (unpublished).

¹¹CDHSW Collaboration, J. P. Berge *et al.*, Report No. CERN-EP/89-103, 1989 (unpublished).

¹²WA70 Collaboration, M. Bonesini *et al.*, Z. Phys. C **38**, 371

- (1988).
- ¹³E605 Collaboration, C. N. Brown *et al.*, Phys. Rev. Lett. **63**, 2637 (1989).
- ¹⁴CDHSW Collaboration, H. Abramowitz *et al.*, Z. Phys. C **15**, 19 (1982); CCFR Collaboration, C. Foudas *et al.*, Phys. Rev. Lett. **64**, 1207 (1990); see also F. Sciulli, in *Proceedings of the 1985 International Symposium on Lepton and Photon Interactions at High Energies*, Kyoto, Japan, 1985, edited by M. Konuma and K. Takahashi (RIFP, Kyoto University, Kyoto, 1986), p. 8.
- ¹⁵A. D. Martin, R. G. Roberts, and W. J. Stirling, Phys. Lett. B **228**, 149 (1989).
- ¹⁶EMC Collaboration, J. J. Aubert *et al.*, Nucl. Phys. **B213**, 31 (1983).
- ¹⁷P. Aurenche, R. Baier, M. Fontannaz, J. F. Owens, and M. Werlen, Phys. Rev. D **39**, 3275 (1989).
- ¹⁸P. M. Stevenson and H. D. Politzer, Nucl. Phys. **B277**, 758 (1986); P. Aurenche, R. Baier, M. Fontannaz, and D. Schiff, *ibid.* **B296**, 509 (1987); **B297**, 661 (1988).
- ¹⁹P. Aurenche and M. R. Whalley, Durham-RAL HEP Database Report No. RAL-89-106, 1989 (unpublished).
- ²⁰A. D. Martin, R. G. Roberts, and W. J. Stirling, Phys. Lett. B **189**, 220 (1987).
- ²¹D. W. Duke and J. F. Owens, Phys. Rev. D **30**, 49 (1984).
- ²²UA2 Collaboration, J. Alitti *et al.*, Report No. CERN-EP/90-20, 1990 (unpublished).
- ²³CDF Collaboration, P. Derwent, in Proceedings of the XXV Rencontre de Moriond, 1990 (unpublished).
- ²⁴L. V. Gribov, E. M. Levin, and M. G. Ryskin, Nucl. Phys. **B188**, 555 (1981); J. Kwiecinski, Z. Phys. C **29**, 147 (1985); J. Collins and J. Kwiecinski, Nucl. Phys. **B316**, 307 (1989).
- ²⁵The distributions can be obtained by electronic mail from WJS@UK.AC.DUR.HEP.
- ²⁶E. Eichten, I. Hinchliffe, K. Lane, and C. Quigg, Rev. Mod. Phys. **56**, 579 (1984).
- ²⁷M. Diemoz, F. Ferroni, E. Longo, and G. Martinelli, Z. Phys. C **39**, 21 (1988).
- ²⁸J. Blümlein, M. Klein, Th. Naumann, and T. Riemann, in *Proceedings of the Workshop on Hadron Electron Ring Accelerator*, edited by R. D. Peccei (DESY, Hamburg, Germany, 1988), Vol. 1, p. 67.
- ²⁹J. Blümlein, G. Ingelman, M. Klein, and R. Rückl, Z. Phys. C **45**, 501 (1990).